An Unprecedented Co^{II} Cuboctahedron as the Secondary Building Unit in a Co-based Metal-Organic Framework

Rebecca J. Holmberg, Marika Kay, Eugene Kadantsev, Peter Boyd, Tomoko Aharen, Serge Desgreniers, Tom K. Woo, Muralee Murugesu*

Department of Chemistry, University of Ottawa, 10 Marie Curie Private, Ottawa, ON, Canada K1N 6N5. E-mail: m.murugesu@uottawa.ca; Fax: +1 (613) 562 5170, Tel: +1 (613) 562 5800 ext. 2733

Supporting Information:

Experimental Section

Materials and Physical Measurements.

All manipulations were performed under aerobic/ambient conditions. All reagents were purchased from the following sources: Alfa Aesar, Acros Organics, Strem Chemicals, J. T. Baker and Sigma Aldrich. All reagents were employed without further purification.

4-(4'-carboxyphenyl)-1,2,4-triazole (Hcpt) Ligand synthesis closely followed the method previously reported by our group.[S1] Formylhydrazide (90 %, 0.11 g, 1.9 mmol) with ethanol (5 mL, 99 %) was placed in a microwave tube. After dissolution, triethylorthoformate (TEOF, 0.47 mL, 1.9 mmol) was added and the sealed tube was mounted in a Biotage initiator microwave. After 5 min at 150 °C and 10 bars of pressure, a clear solution was obtained. 4-aminobenzoic acid (0.25 g, 1.8 mmol) was added immediately after the first reaction (formation of diformylhydrazide) and the vial was placed back in the microwave. The reaction conditions for the formation of Hcpt were the same as the previous step. The beige-white powder was obtained in a slightly pink solution and the product was purified by recrystallisation in 10 mL of hot dimethylformamide (DMF). After recrystallisation, the product was washed with diethyl ether. Hcpt was obtained as fine, shiny white powder (110mg, 30%), the purity of which was checked by ^{1}H NMR and compared the reported data (d^6-DMSO, 400 MHz): δ(ppm) 13.20 (s, 1H), 9.21 (s, 2H), 8.06 (d, J = 8.8 Hz, 2H), 7.83 (d, J = 8.8 Hz, 2H). Yield: 25%. Selected FTIR (cm^{-1}) ν = 3112, 2455, 1894, 1685, 1608, 1321, 1245.

[Co$^{II}_8$(OH)$_6$(cpt)$_{12}$][CoCl$_4$] (Co-MOF3) A mixture of Hcpt (58.5 mg, 0.31 mmol) and Co(NO$_3$)$_2$·6H$_2$O (220 mg, 0.75 mmol), was placed in an autoclave Teflon bomb (20 mL) along with a mixture of solvents composed of DMF (10 mL), EtOH (99 %, 3 mL), and water (0.3 mL). HCl (10M, 0.1mL) was added to the mixture and the vial was sealed. The vial was kept at 150 °C for 24 hours, followed by cooling at a rate of 6.54 min / °C yielding spherical dark blue cubic

crystals (Figure S1) (126 mg). Selected FTIR (cm^{-1}) ν = 3384(br), 3099(m), 2359(m), 1656, 1601, 1566, 1408, 1315, 1250.

NMR NMR analyses were conducted using the Bruker Avance 400 MHz spectrometer equipped with an automatic sample charger and a 5, auto-tuning broadband probe with Z gradient.

Infrared and Raman Spectrometry   Infrared spectra were recorded on all samples in the solid state on a Nicolet 6700 FT-IR spectrometer in the 4000-600 cm^{-1} region. Raman spectra were recorded on single crystals of Co-MOF3 using a custom setup. The laser wavelengths were 488 and 532 nm, and spectra were recorded in the 3500-0 cm^{-1} region.

X-Ray Crystallography   Single crystal X-Ray diffraction experiments were performed on a Bruker AXS SMART single crystal diffractometer with a sealed Mo tube APEX II CCD detector, which was used to collect the unit cell and intensity data using graphite Mo-Kα radiation (λ = 0.71073 Å). Data reduction included correction for Lorentz and polarisation effects, with an applied multi-scan absorption correction (SADABS). Crystal structures were solved and refined using SHELXTL. All non-hydrogen atoms were refined with anisotropic thermal parameters. Hydrogen atom positions were calculated geometrically, and were riding on their respective atoms. Partially occupied water molecules were localized and modelled during refinement (as mentioned in the main text). Refinement revealed multiple electron density peaks of roughly 1/12 of a carbon atom (0.53 electrons).

X-ray Powder Diffraction (XRPD) experiments were performed using a RIGAKU Ultima IV, equipped with a Cu-Kα radiation source (λ = 1.541836 Å), and a graphite monochromator. Scanning of the 2θ range was performed from 5-40°. In order to assign the peaks corresponding to particular crystalline phases, PDXL software equipped with the RIGAKU apparatus was used with the ICDD database. XRPD pattern was consistent in 2θ values with the generated pattern from XRD, with slight discrepancies in some intensities of peaks attributed to preferred orientation due to limited sample size.

SEM Scanning electron microscopy (SEM) images were taken of single crystals using a JSM-7500F FESEM (JEOL).

TGA Thermo-gravimetric analysis (TGA) data were recorded using an SDT 2960 Simultaneous DSC-TGA, TGA Q5000 V3.13 Build 261 instrument. The analysis was carried out under air flow (20 mL min^{-1}) with a heating rate of 10 °C min^{-1} from room temperature up to 800 °C, with complementary nitrogen flow (100 mL min^{-1}) as a protective gas.

SQUID   Magnetic measurements were performed using a Quantum Design SQUID magnetometer MPMS-XL7, operating between 1.8 and 300 K for dc-applied fields ranging from -7 to 7 T. Susceptibility measurements were performed on the freshly filtered, crushed crystalline Co-MOF3 (23.6 mg), wrapped within a polyethylene membrane. The field dependent magnetisation data of Co-MOF3 was also collected at 1.8, 3, 5, and 7 K under applied fields up to 7 T. The magnetisation data were initially collected at 100 K to check for ferromagnetic impurities, found to be absent in all samples.

Supplemental Figures
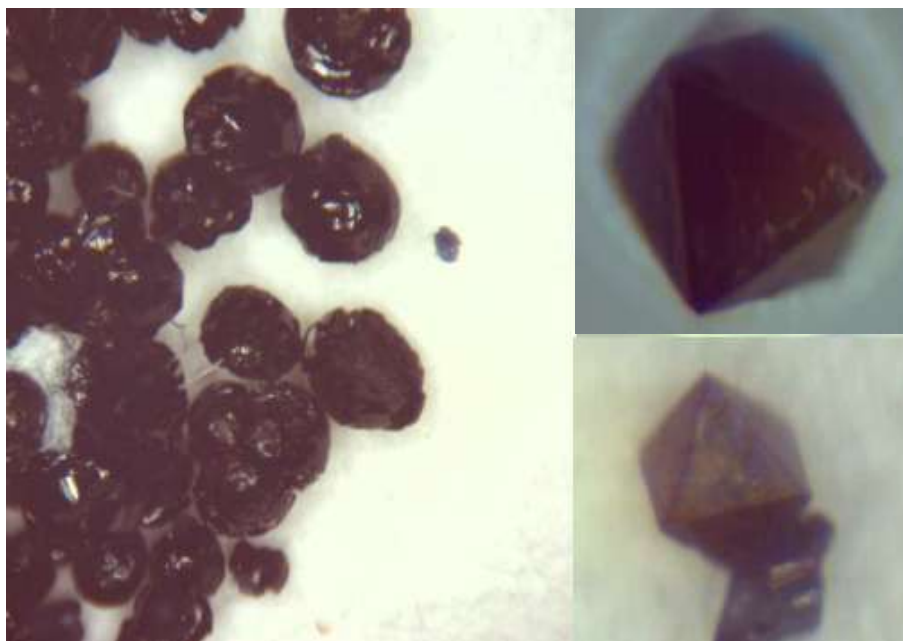
Figure S1. Co-MOF3 blue cubic crystals observed under a microscope. Bulk crystals were vacuum filtered on the left and placed in paraffin oil on the right.

Figure S2. Co-MOF3 blue cubic crystals observed under a scanning electron microscope. Scale bar: 100µm.

Table S1. Crystallographic data for Co-MOF3.

Compound	Co-MOF3
Empirical formula	$C_{13.5}H_{14.5}Cl_2Co_{2.5}N_{4.5}O_{6.5}$
Formula weight (g/mol)	562.06
Crystal system	cubic
Space group	F23 (no. 196)
Temperature (K)	200(2)
Crystal size (mm)	0.15 x 0.11 x 0.10
Z	16
a (Å)	23.3565(6)
b (Å)	23.3565(6)
c (Å)	23.3565(6)
α (°)	90.00(6)
β (°)	90.00(6)
γ (°)	90.00(6)
Volume ($Å^3$)	12741.58(57)
Calculated density (gcm^{-3})	1.17185
Absorption coefficient (mm^{-1})	1.487
F(000)	4488
Θ range for data collection (°)	2.47 - 30.49
Limiting indices	$h = \pm31, k = \pm28, l = \pm33$
Reflections collected/unique	55588/3203
R(int)	0.0294
Completeness to $\theta = 30.49$ (%)	0.99
Max. and min. Transmission	0.8077 and 0.8655
Data/restraints/parameters	3203/6/65
Goodness-of-fit on F^2	1.046
Final R indices [$I.2\sigma(I)$]	$R_1 = 0.0512$, w$R_2 = 0.1138$
R indices (all data)	$R_1 = 0.0632$, w$R_2 = 0.1182$
Largest diff. Peak/hole, $eÅ^{-3}$	0.489 and -0.693

Table S2. Select bond distances for Co-MOF3.

Bond	Distance (Å)
Co1—O3^{i}	2.048(10)
Co1—O3^{ii}	2.048(10)
Co1—O3^{iii}	2.048(10)
Co1—N3^{iv}	2.110(14)
Co1—N3^{v}	2.110(14)
Co1—N3	2.110(14)
Co1—O1^{v}	2.1944(10)
Co1—O1^{vi}	2.1944(10)
Co1—O1	2.1944(10)
Co1—Co2	2.9985(4)
Co1—Co2^{vii}	2.9985(4)
Co1—Co2^{viii}	2.9985(4)
Co2—O2^{ix}	2.030(9)
Co2—O2^{x}	2.030(9)
Co2—O2^{i}	2.030(9)
Co2—N2	2.065(14)
Co2—N2^{xi}	2.065(14)
Co2—N2^{xii}	2.065(14)
Co2—O1^{viii}	2.1943(11)
Co2—O1^{vi}	2.1943(11)
Co2—O1^{v}	2.1943(11)
Co2—Co1^{vii}	2.9985(4)
Co2—Co1^{viii}	2.9985(4)
O1—Co1^{xvii}	2.1944(10)
O1—Co2^{viii}	2.1944(11)
O1—Co2^{vii}	2.1944(11)
O2—Co2^{i}	2.030(9)
O3—Co1^{i}	2.048(9)

(i) 1.5-x, y, 1.5-z; (ii) 1-y, -0.5+z, 1.5-x; (iii) 1.5-z, -0.5+x, 1-y; (iv) 1-y, 1-z, x; (v) z, 1-x, 1-y; (vi) 1-y, z, 1-x; (vii) x, 1-y, 1-z; (viii) 1-x, 1-y, z; (ix) 1.5-z, 1.5-x, y; (x) y, 1.5-z, 1.5-x; (xi) y, z, x; (xii) z, x, y; (xiii) x, 0.5-y, 1.5-z; (xiv) 1.5-x, 0.5-y, z; (xv) x, 0.5-y, 0.5-z; (xvi) 1.5-x, y, 0.5-z; (xvii) 1-x, y, 1-z; (xviii) 1.5-z, x, 1.5-y.
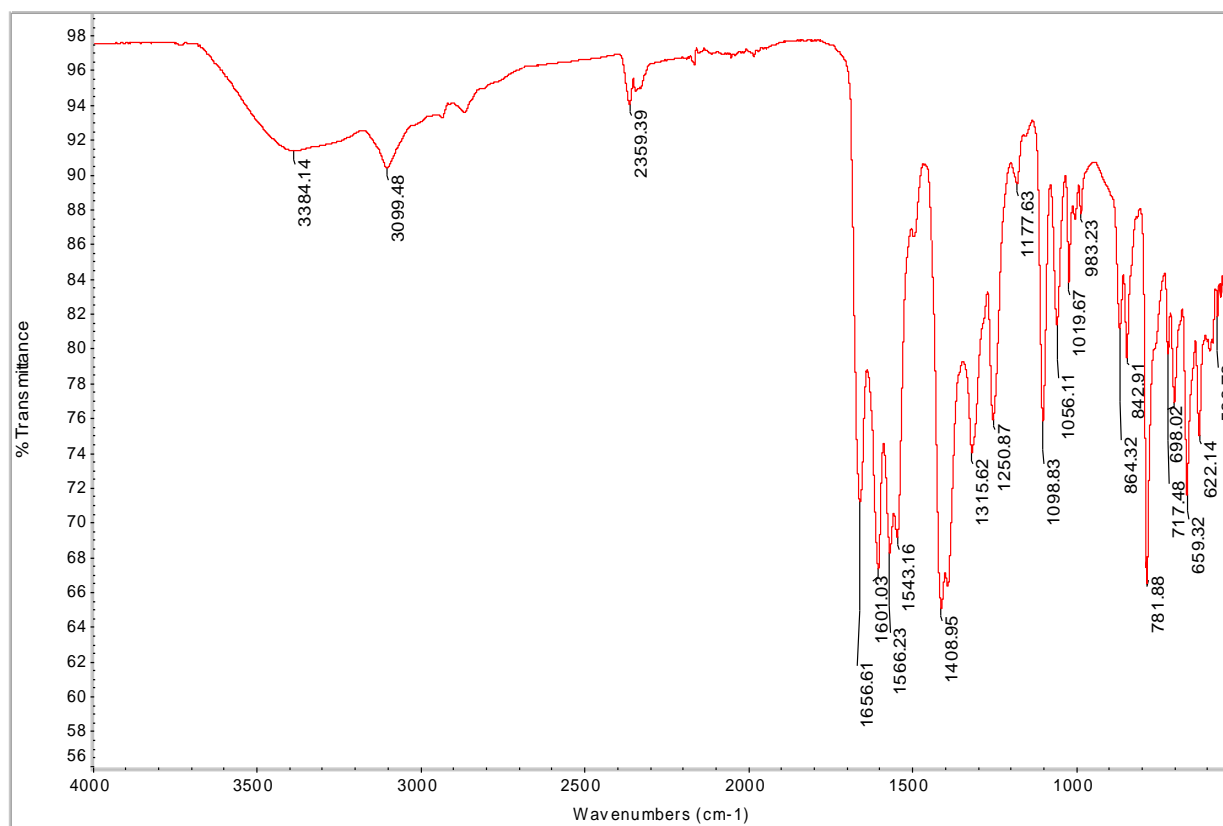
Figure S3. FTIR spectra of Co-MOF3 for vacuum filtered crystals in the 4000-600 cm^{-1} region.
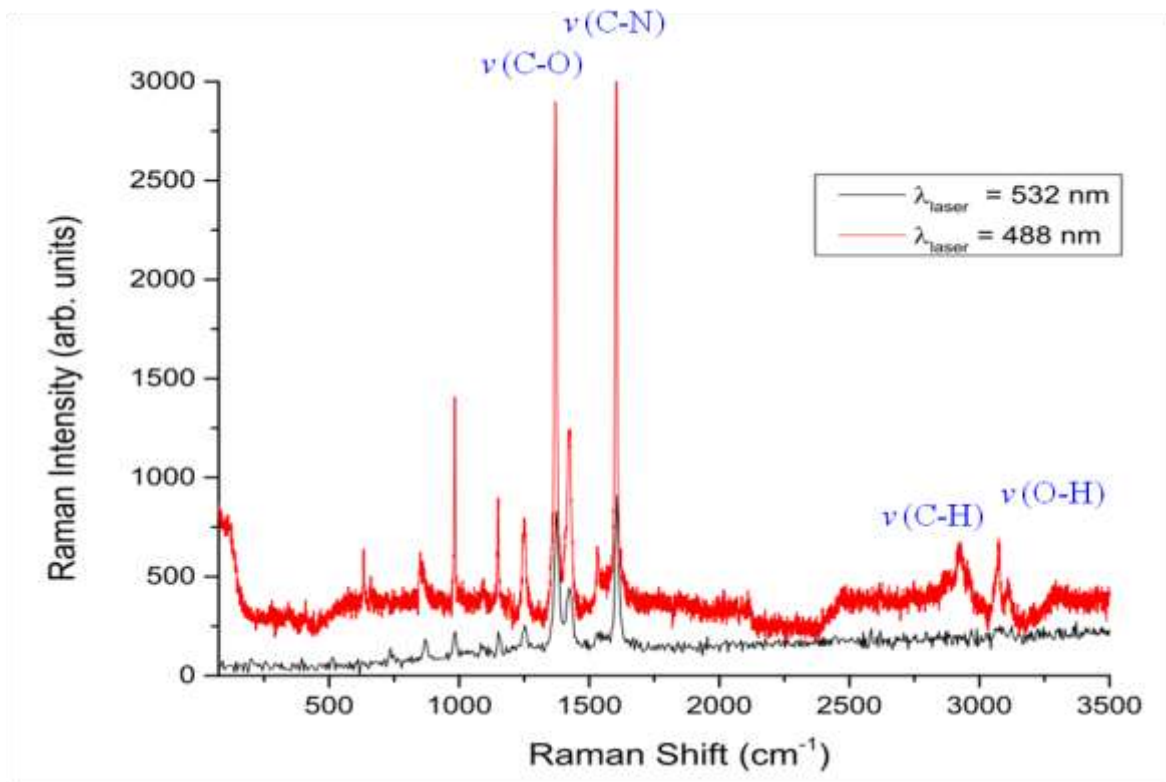
Figure S4. Raman spectra of Co-MOF3 for air dried single crystals in the 3500-0 cm^{-1} region.
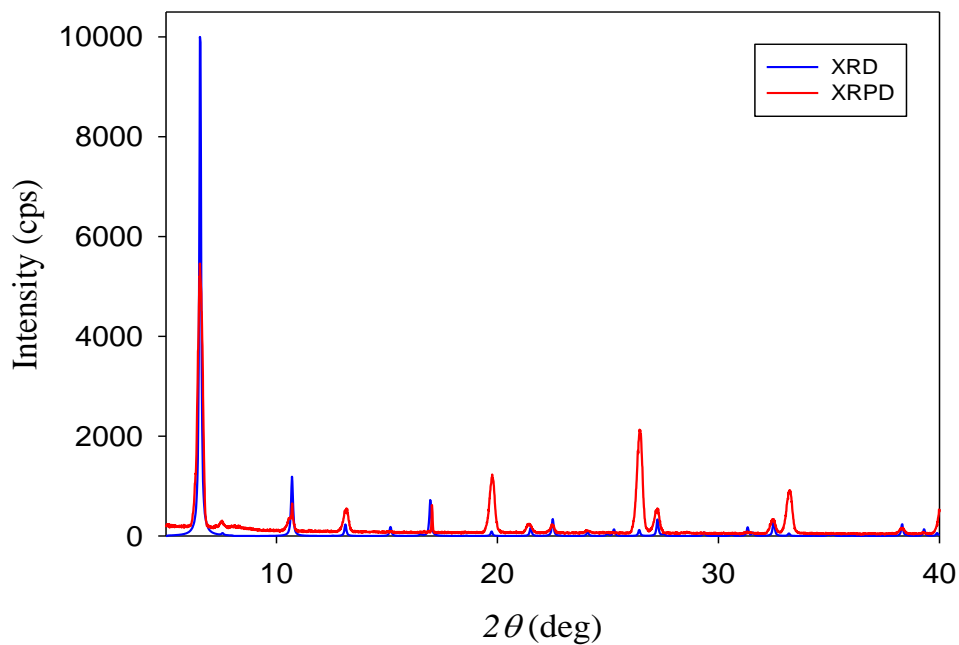
Figure S5. X-ray powder diffraction spectra of Co-MOF3 for air dried single crystals in the 5-40° 2θ region.
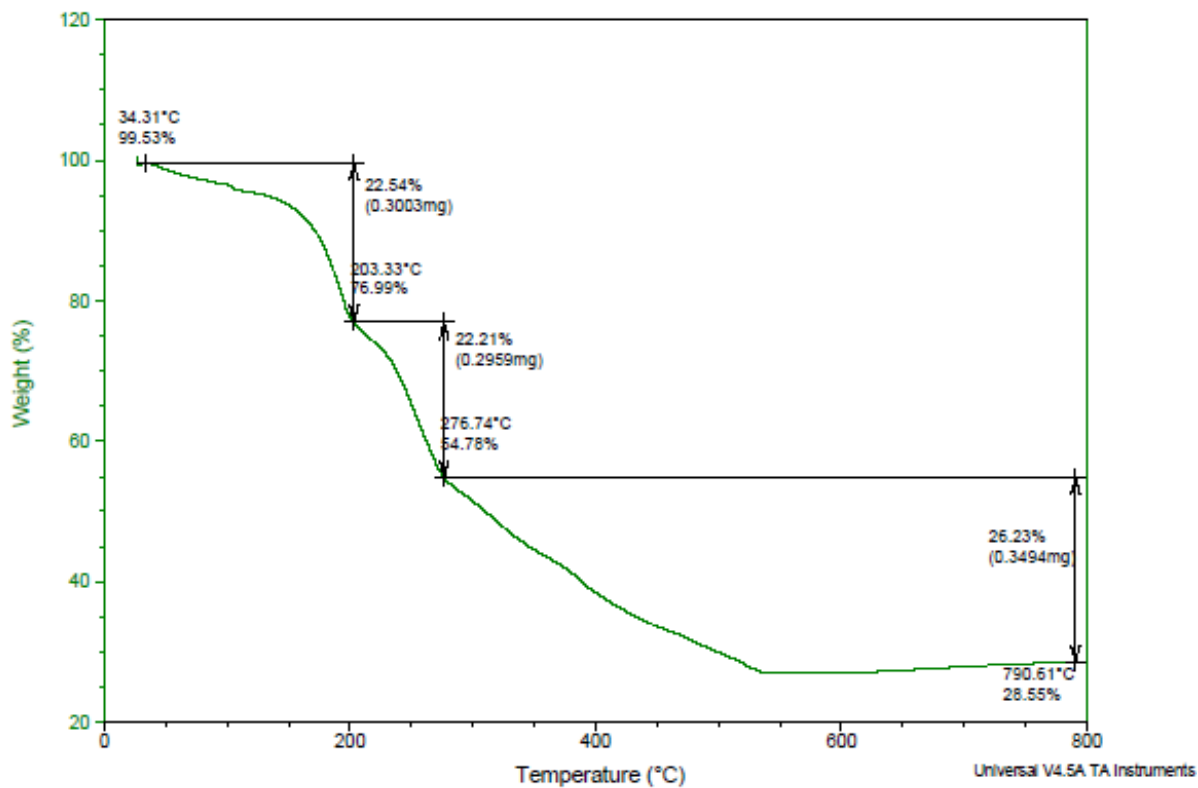
Figure S6. TGA spectra for vacuum filtered Co-MOF3 crystals.
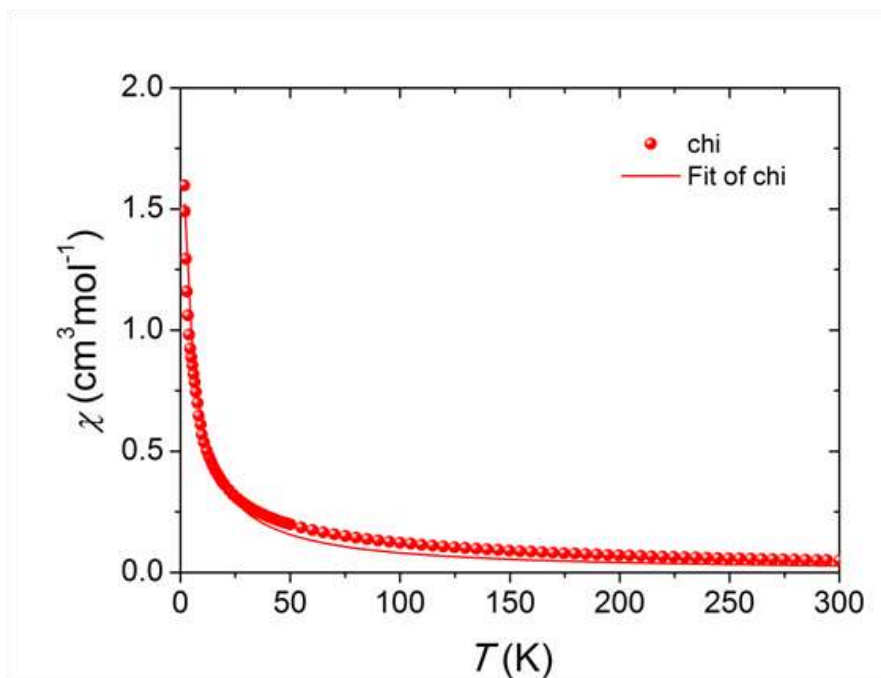
Figure S7. Temperature dependence of χ at 1000 Oe for Co-MOF3. Solid line represents Curie-Weiss fitting of data.
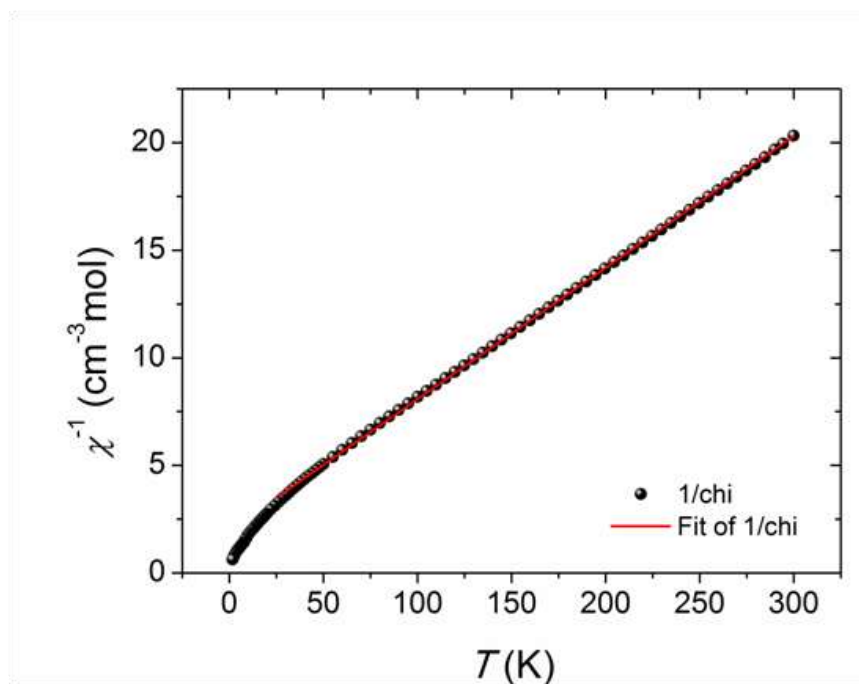
Figure S8. Temperature dependence of χ^{-1} at 1000 Oe for Co-MOF3. Solid line represents Curie-Weiss fitting of data.
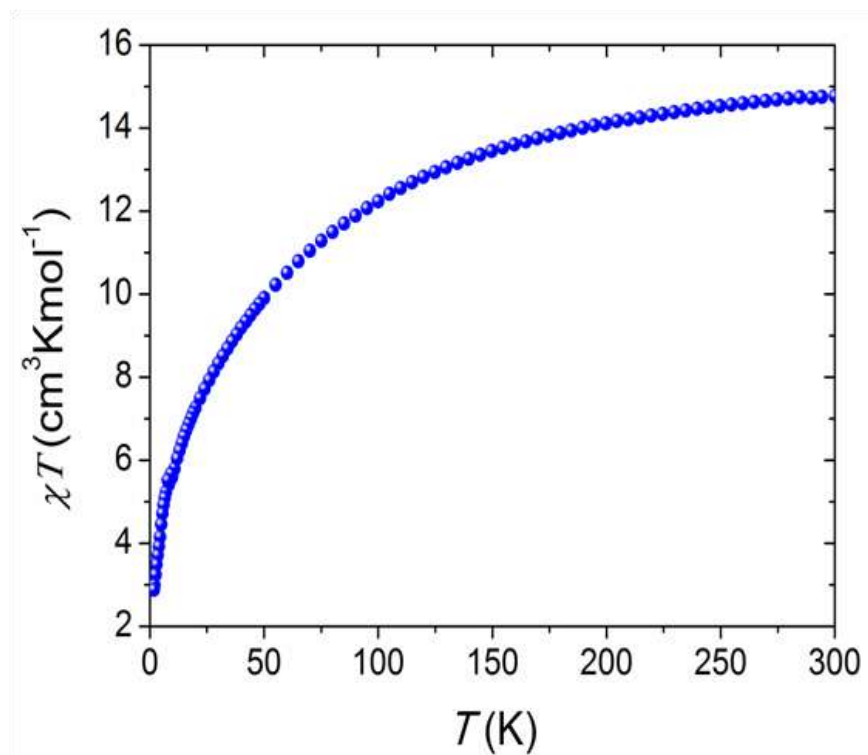
Figure S9. Temperature dependence of the χT product at 1000 Oe for Co-MOF3.
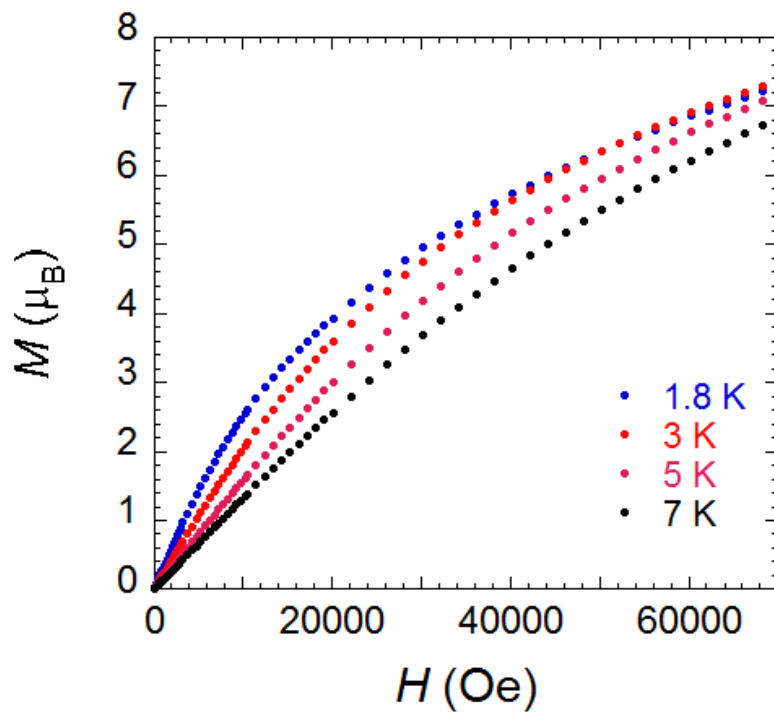
Figure S10. Field dependence of the magnetisation of Co-MOF3 at indicated temperatures.
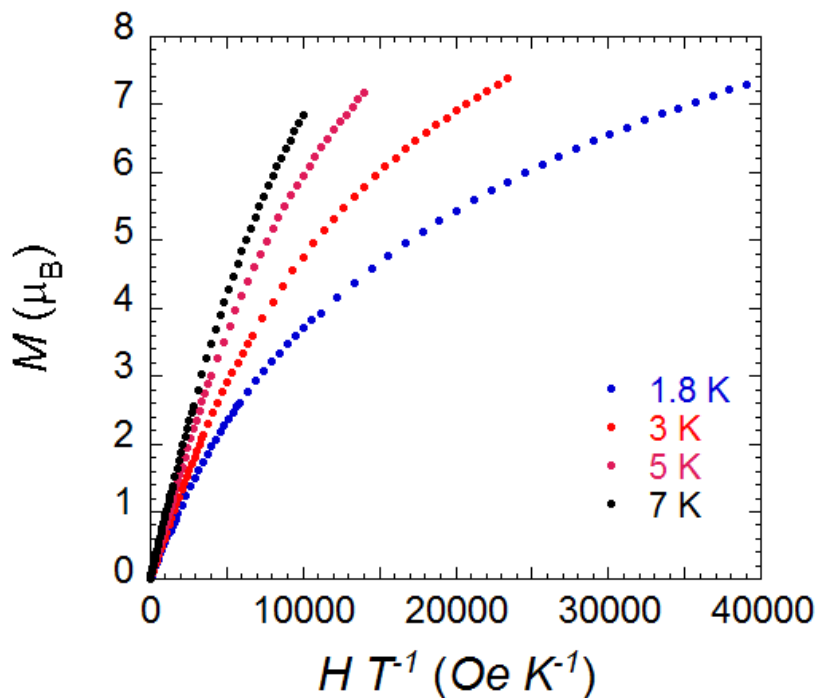
Figure S11. *M* vs. *HT*$^{-1}$ plot for Co-MOF3 at indicated temperatures.

Computational Details

The periodic density functional theory (DFT)[S2-S3] calculations were performed with the VASP code,[S4-S6] using the PBE exchange-correlation functional.[S7] A plane wave basis set with PAW[S8-9] pseudopotentials was utilized with a kinetic energy cut-off of 400 eV. The reciprocal space was sampled with a single Γ-point. All calculations reported were spin polarized. Initial guess of the various magnetic moments on the Co atoms was obtained using MAGMOM option within VASP. The initial magnetic moments on Co atoms were set to ±3 Bohr magnetons. The converged self-consistent spin-unpolarized wave-function was used as an initial guess in the spin polarized calculations. We also employed Gaussian smearing with a smearing parameter set to 0.1 eV, Davidson/RMM-DIIS algorithm for the diagonalization of the Kohn-Sham Hamiltonian (ALGO=Fast option within VASP), and a reduced "mixing" parameter (AMIX_MAG = 0.8 option within VASP).

The exact arrangement of the asymmetric cpt⁻ ligands around each cubane cluster could not be determined definitively, due to the cpt⁻ ligand disorder in the single crystal X-ray studies. In other words, exactly where the O- or N-end of the cpt⁻ ligand binds to the edge of the Co cluster is not known experimentally. For the DFT calculations, two configurations were explored. The first, as shown in Figure 1b, is constructed such that if one cubane edge coordinates to the O-end of a cpt- ligand, the opposite edge of the cubane cluster coordinates to the N-end of a cpt⁻ ligand.

This configuration allows for a simulation cell to be constructed that contains a single 8 cubane SBU and only contains 150 atoms (including 2 $CoCl_4$ counter ions). We will denote this as the asymmetric model. In this model, half of the Co atoms are coordinated to 5 oxygens (3 μ_4 O and two carbooxylate oxygens) and 1 nitrogen and another half of Co atoms are coordinated with 4 oxygens (3 μ_4 oxygens and one carbooxylate oxygen) and two nitrogens. The second configuration is shown in Figure 1a, and is constructed such that each opposing cubane edge coordinate to the same end of a cpt$^-$ ligand. This second configuration requires a simulation cell which is 4 times larger and contains 4 cubane SBUs and 600 atoms (including 8 $CoCl_4$ counter ions). We will denote this as the symmetric model. In the symmetric model, each Co of the inorganic SBU is coordinated with 4 oxygens and 2 nitrogens.

For the discussion of energies presented in the main text of this work, we used the results obtained for the asymmetric model, where the geometry was fixed to that of the single crystal X-ray structure. Our conclusions hold qualitatively for the symmetric model as well. Figure S12 shows the energy spectra of the anti-ferromagnetic solutions in the primitive unit cell and total magnetization per cell in Bohr magnetons (μB). The energies of the anti-ferromagnetic solutions are given with respect to the energy of the ferromagnetic solution. Figure S12 reveals that the most stable anti-ferromagnetic solution (anti-ferromagnetic ground state) lies 4.5 kcal/mol below the ferromagnetic solution. We find that the total integrated spin-polarization in this anti-ferromagnetic ground state is almost zero due to the cancellation of magnetic moments on the Co atoms (which were found to be ~±2.4 μB). This contrasts, the total magnetization in the ferromagnetic state is, which is calculated to be approximately 20 μB. We have also examined spin-density in the anti-ferromagnetic ground state and several excited anti-ferromagnetic configurations. We find that the anti-ferromagnetic ground state corresponds to the parallel arrangement of magnetic moments on the "same facet" of 8 atom Co inorganic SBU (top right of Figure S12). On the other hand, the most unstable anti-ferromagnetic configuration which lies, approximately, 13.5 kcal/mol above the ferromagnetic solution, corresponds to the arrangement of parallel magnetic moments located in the opposite corners of 8 atom Co SBU (like hydrogen atoms in CH_4). This most unstable anti-ferromagnetic solution is shown in the bottom right corner of Figure S12). The parallel spins in this configuration cannot interact directly via Co-Co bond as in the anti-ferromagnetic ground state and, as a result, this configuration becomes highly destabilized.
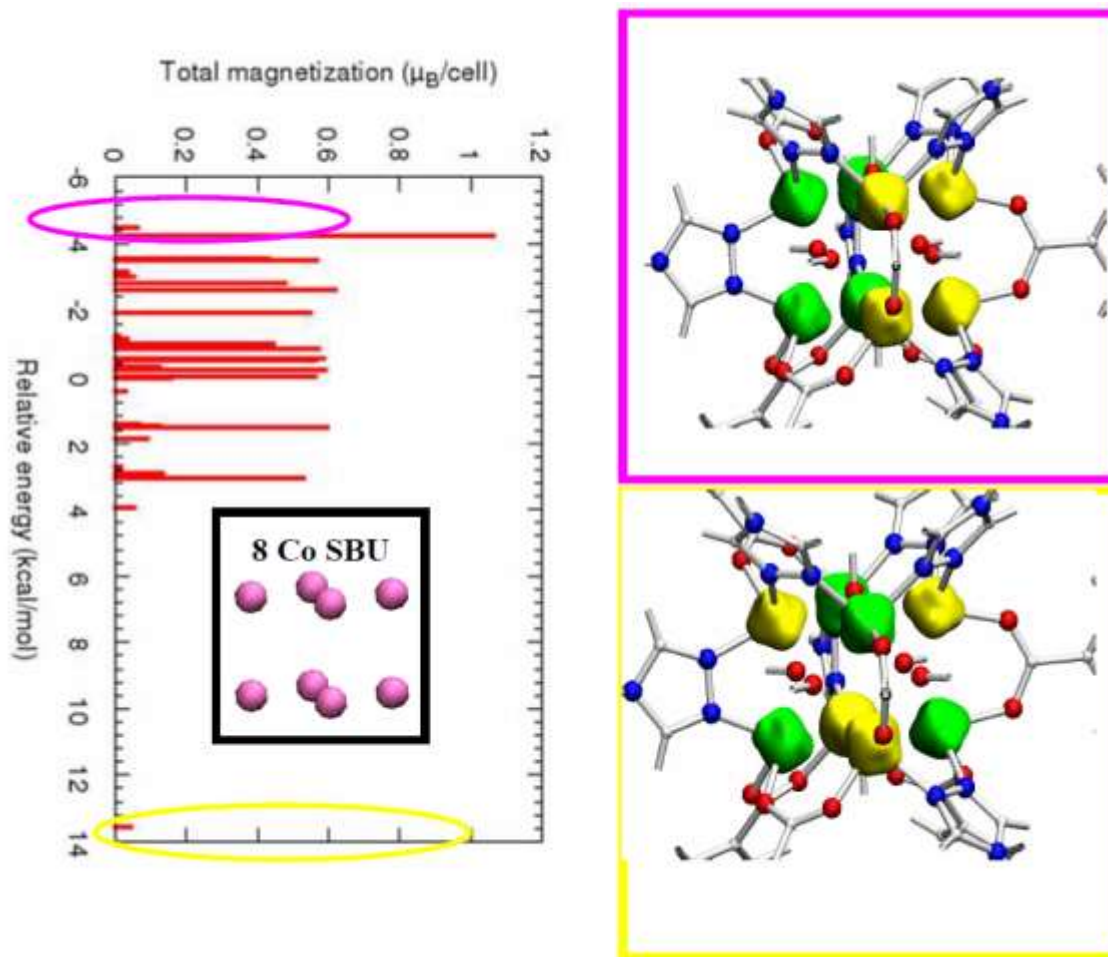
Figure S12. The energy spectrum (left) of the anti-ferromagnetic solutions relative to the ferromagnetic ground state in a primitive unit cell containing one 8 atom Co SBU. Isosurface of the spin density difference in the anti-ferromagnetic ground state (top right) and most excited anti-ferromagnetic state (bottom right). The magnetization is localized on Co atoms. The green (yellow) isosurfaces correspond to the regions with dominant spin-up (or down) component.

To further validate our results, we have also performed the same calculations with the symmetric model where each opposing cubane edge coordinates to the same end of a cpt⁻ ligand. These calculations are very computationally demanding as one needs to consider a larger 600 atom supercell. For this larger supercell, we find that relative to the ferromagnetic solution, the lowest energy anti-ferromagnetic state is determined to be 4.6 kcal/mol lower in energy than the ferromagnetic state. This is in excellent agreement to the results obtained with the asymmetric model where the ground state was found to be 4.5 kcal/mol lower in energy than the ferromagnetic state. As a further validation of the calculations, we have also repeated the calculations on the smaller asymmetric model whereby the geometry was optimized in the ferromagnetic state and the lowest energy anti-ferromagnetic state. We found, once again, that

the anti-ferromagnetic configuration was energetically preferable and that he energy difference was 5.5 kcal/mol.

The gas adsorption isotherms, void fraction, and surface area calculations presented here were performed on the asymmetric model. The physical properties relating to the available pore space in Co-MOF3 were invariant with respect to how the cpt⁻ ligands coordinate to the cuboctahedral Co clusters.

Grand Canonical Monte Carlo calculations were performed to evaluate the CO_2 and N_2 adsorption isotherms. During these calculations the framework was held fixed while gas molecules were assumed rigid, such that the guest-host interaction energies were calculated as a sum of non-bonded interactions. The electrostatic component was determined by partial atomic charges assigned to atoms on the framework and gas molecules. The partial atomic charges on the framework atoms were calculated with the REPEAT method[S10] using the electrostatic potential defined from the lowest energy spin polarized configuration reported above. The dispersive and steric repulsive interactions were defined using an isotropic 12-6 lennard jones (L-J) potential at each atom-centre. The ε and σ parameters defining atom-specific L-J functions were taken from the universal force field (UFF).[S11] Heteroatomic L-J interactions were computed using the Lorentz-Berthelot mixing rules.

The parameters defining the interactions of the gas molecules are defined in Table S3, which for N_2 are taken from the TraPPE force field[S12] and CO_2 were taken from the work of García-Sánchez et al.[S13]

Table S3: Guest force field parameters

Parameter	N (N_2)	E* (N_2)	C (CO_2)	O (CO_2)
q (e)	-0.482	+0.964	+0.6512	-0.3256
ε (kcal)	0.07154	0.0	0.05948	0.17023
σ (Å)	3.3100	0.0	2.745	3.017
R (Å)	0.550 (N---E)		1.149 (C---O)	

* The ghost atom E is defined at the centre of mass of the N_2 molecule

The void volume (0.18 cm³/g) and surface area (1201 m²/g) were calculated with the Zeo++ code,[S14,S15] using probe radii (1.82 Å) corresponding to N_2 gas molecules. All calculations were performed with the $CoCl_4$ counter-ions in the pores to provide a neutral framework.
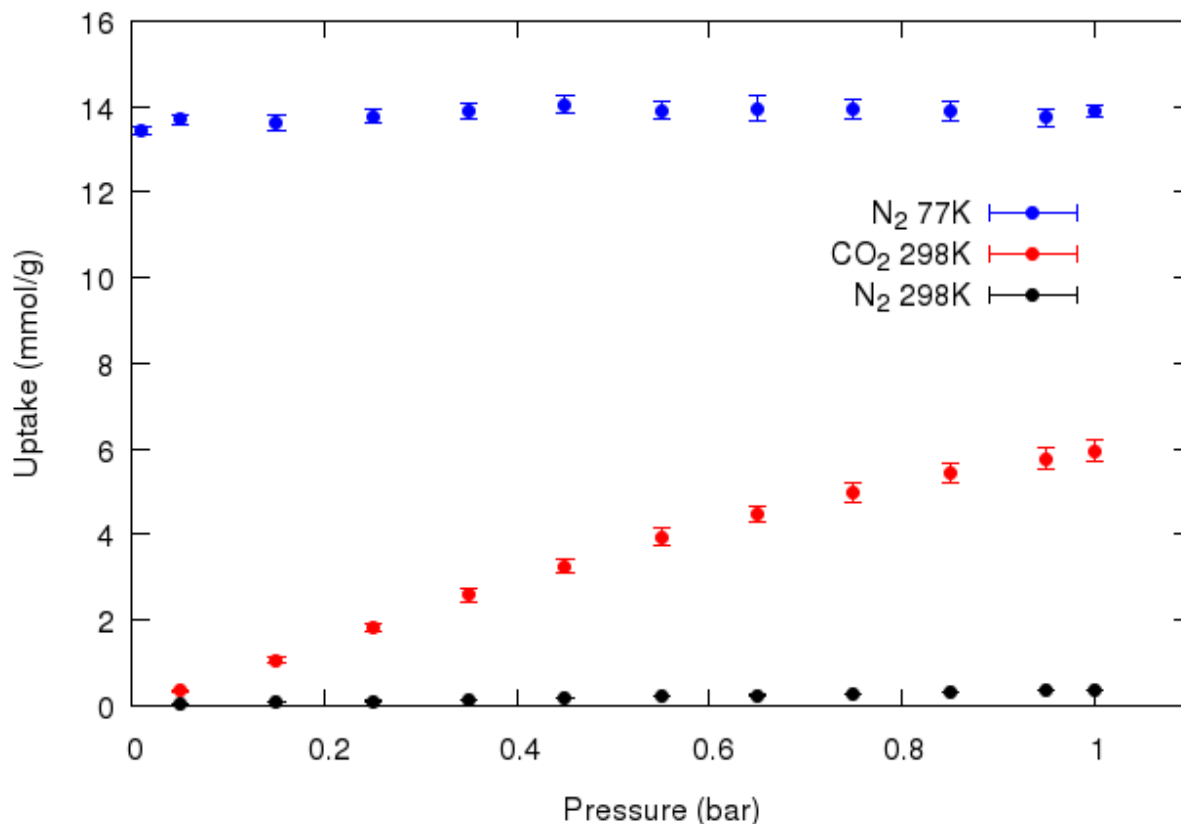
Figure S13: Gas adsorption isotherms for CO_2 and N_2. y-error bars denote the standard deviation in the uptake values associated with the statistical sampling of the grand canonical ensemble.

References

S1. D. Savard, P. H. Lin, T. J. Burchell, I. Korobkov, W. Wernsdorfer, R. Clérac and M. Murugesu, *Inorg. Chem.*, 2009, **48**, 11748.

S2. P. Hohenberg, W. Kohn, *Phys. Rev.*, 1964, **136**, B864.

S3. W. Kohn, L. J. Sham, *Phys. Rev.*, 1965, **140**, A1133.

S4. G. Kresse, J. Furthmuller, *Phys. Rev. B*, 1996, **54**, 11169.

S5. G. Kresse, J. Hafner, *Phys. Rev. B*, 1993, **47**, 558.

S6. G. Kresse, J. Hafner, *Phys. Rev. B* 1994, **49**, 14251.

S7. J. P. Perdew, K. Burke, M. Ernzerhof, *Phys. Rev. Lett.*, 1996, **77**, 3865.

S8. P. E. Blochl, *Phys. Rev. B*, 1994, **50**, 17953.

S9. G. Kresse, D. Joubert, *Phys. Rev. B*, 1999, **59**, 1758.

S10. C. Campañá, B. Mussard, and T. K. Woo, *J. Chem. Theory Comput.*, 2009, **5**, 2866–2878.

S11. A. K. Rappe, C. J. Casewit, K. S. Colwell, W. A. Goddard, and W. M. Skiff, *J. Am. Chem. Soc.*, 1992, **114**, 10024–10035.

S12. J. J. Potoff and J. I. Siepmann, *AIChE J.*, 2001, **47**, 1676–1682.

S13. A. García-Sánchez, C. O. Ania, J. B. Parra, D. Dubbeldam, T. J. H. Vlugt, R. Krishna, and S. Calero, *J. Phys. Chem. C*, 2009, **113**, 8814–8820.

S14. T. F. Willems, C. H. Rycroft, M. Kazi, J. C. Meza, and M. Haranczyk, *Microporous Mesoporous Mater.*, 2012, **149**, 134–141.

S15. R. L. Martin, B. Smit, and M. Haranczyk, *J. Chem. Inf. Model.*, 2012, **52**, 308–18.